JOURNAL OF PROPULSION AND POWER
Vol. 21, No. 4, July–August 2005

Off-Design Transonic Rotor–Inlet Guide Vane Unsteady Aerodynamic Interactions

John Papalia,* Patrick B. Lawless,† and Sanford Fleeter‡
Purdue University, West Lafayette, Indiana 47907

The unsteady aerodynamic interactions of a transonic rotor with an upstream inlet guide vane (IGV) row under off-design operating conditions are investigated. The rotor-generated IGV unsteady aerodynamics are quantified when the IGV reset angle causes the rotor to be on the verge of becoming transonic and the vane exit metal angle is nearly aligned with the detached rotor shocks, that is, at the vane maximum modal force excitation. This is accomplished through experiments in a $1\frac{1}{2}$-stage axial-flow compressor, with detailed data acquired and analyzed. These data define the 90% span transonic rotor–generated forcing function to the IGVs, the resulting vane steady and unsteady aerodynamic response, and the time-variant vane-to-vane flow field over one interaction cycle.

Nomenclature

C	=	vane chord
f	=	frequency
f_{BP}	=	blade-pass frequency
M_{abs}	=	absolute Mach number
M_{rel}	=	relative Mach number
N_c	=	corrected rotor speed
p	=	unsteady vane static surface pressure
p'_s	=	unsteady static pressure fluctuation due to forcing function
$P_{t,in}$	=	compressor inlet total pressure
T	=	blade-pass period
t	=	time
x	=	chordwise location
y	=	tangential location

Introduction

A TRANSONIC rotor operates with a supersonic relative velocity and a subsonic absolute velocity. Shocks thus form near the rotor blade leading edges and propagate into an upstream vane row. The vane surfaces reflect and diffract these incident shocks in a complex manner, with a time-dependent wave pattern established in the vane passages due to these periodic interactions. For nominal operating conditions near peak efficiency, Fig. 1, rotor–inlet guide vane (IGV) interactions in a $1\frac{1}{2}$-stage transonic compressor have been experimentally investigated.[1,2]

Unfortunately, compressors do not always operate near peak efficiency. Rather, they operate over a wide range of inlet conditions, including off-design conditions where the incidence differs considerably from that near peak efficiency. Variable stators are utilized to improve compressor performance under off-design conditions by restaggering the vanes to reduce the rotor incidence at part speed. Because compressor performance is determined by the corrected operating conditions, a variable inlet vane schedule consists of vane reset angles as a function of corrected rotor speed, as schematically depicted in Fig. 2.

A transonic rotor is a significant source of unsteady aerodynamic excitation to an inlet vane row, with resonant response occurring when the rotor blade-pass frequency coincides with a vane natural frequency. Because compressors operate over a range of inlet conditions, the corrected and mechanical conditions can differ significantly for different missions. Also, because the variable inlet vane stagger reset is determined by the corrected rotor speed, the specific inlet vane stagger angle at the resonant mechanical speed can vary considerably depending on compressor inlet conditions. It should be noted that the majority of blade row interaction resonance issues are under off-design operating conditions where the incidence angles differ greatly from design values, that is, with the rotor not operating near peak efficiency.

Structurally, the forcing function to the upstream vane row is the modal force on the vanes, determined by integrating the in-phase components of the vane surface unsteady pressures and the vibratory displacement. Because the rotor leading edge shocks for transonic flow and the rotor potential field for subsonic flow generate the unsteady pressure loading on the upstream inlet vanes, the modal force driving the vibratory response is strongly dependent on the rotor inlet conditions set by the corrected speed. In fact, the highest inlet vane strains might be expected when the rotor inlet vane reset caused the rotor to be just on the verge of becoming transonic and the IGV trailing edge metal angle was aligned with the detached rotor shocks (Fig. 1). The rotor shocks then "slap" the upstream vanes. Mathematically the forcing function is in-phase with vibratory modes having constant spatial phase, such as first bending, resulting in the maximum possible modal force excitation for these modes.

Time-accurate multiblade row computational fluid dynamics analyses are being utilized to analyze nonlinear blade row interactions; for example, predictions were correlated with the near-peak-efficiency IGV–rotor interaction data.[3–5] These simulation–data correlation results were qualitatively very good, with the detailed correlations somewhat mixed. This is a result, at least in part, of the computational domain being reduced by scaling the geometry so that each airfoil row is represented by a single passage.

This research is directed at investigating the aerodynamic interactions of a transonic rotor with an upstream IGV row under off-design operating conditions. The rotor-generated IGV unsteady aerodynamics are quantified when the IGV reset angle causes the rotor to be on the verge of becoming transonic and the vane exit metal angle is nearly aligned with the detached rotor shocks, that is, at the vane maximum modal force excitation. This is accomplished through experiments in a transonic $1\frac{1}{2}$-stage axial-flow compressor. Detailed data are acquired and analyzed that define the 90% span transonic rotor–generated forcing function to the IGVs, the resulting vane steady and unsteady aerodynamic response, and the time-variant vane-to-vane flow field over one interaction cycle.

Presented as Paper 2002-4220 at the AIAA Joint Propulsion Conference, Indianapolis, 7–10 July 2002; received 6 November 2003; revision received 25 August 2004; accepted for publication 10 October 2004. Copyright © 2004 by the authors. Published by the American Institute of Aeronautics and Astronautics, Inc., with permission. Copies of this paper may be made for personal or internal use, on condition that the copier pay the $10.00 per-copy fee to the Copyright Clearance Center, Inc., 222 Rosewood Drive, Danvers, MA 01923; include the code 0748-4658/05 $10.00 in correspondence with the CCC.

*Graduate Research Assistant, School of Mechanical Engineering.
†Associate Professor, School of Mechanical Engineering. Member AIAA.
‡McAllister Distinguished Professor, School of Mechanical Engineering. Fellow AIAA.

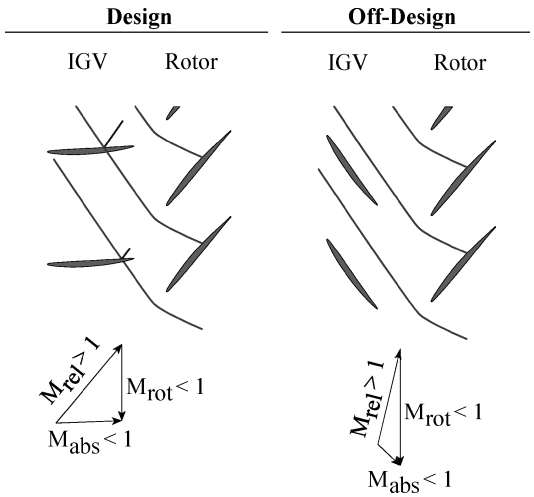

Fig. 1 Rotor–IGV interactions.

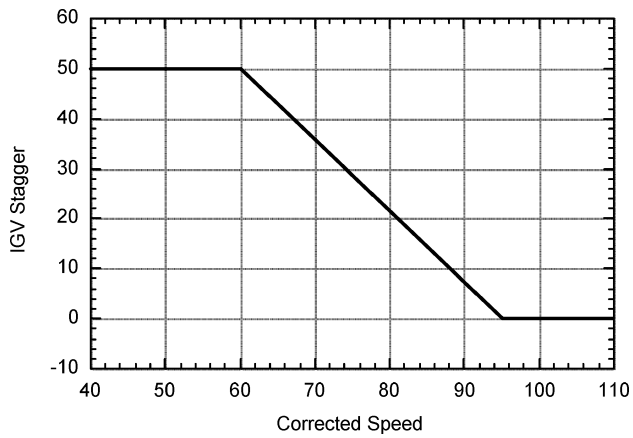

Fig. 2 Typical variable inlet vane schedule.

Research Facility

The Purdue transonic research compressor, depicted in Fig. 3, features a $1\frac{1}{2}$-stage axial-flow geometry representative of those used in the front stages of aircraft engine high-pressure compressors. The drive system consists of a 400-hp ac motor, a variable-speed magnetic clutch, and an 8:1 ratio gearbox, the output of which drives the compressor rotor. Atmospheric air is drawn into the test section through a converging bell-mouth inlet with a 16:1 contraction ratio and exits the test section through discharge piping that contains a butterfly throttle valve to regulate the flow rate.

The test section has a constant hub–tip ratio of 0.67 with a tip diameter of 0.3 m (12.0 in.) and features 18 inlet guide vanes, an integrally bladed rotor with 19 rotor blades, and 18 downstream stator vanes. The rotor blades consist of NACA 65 series profiles on circular arc meanlines with a 5.08-cm (2.0-in.) chord and a thickness distribution varying from 10% at the root to 6% at the tip. The IGV and stator vanes are an advanced controlled diffusion airfoil design with a 4.45-cm (1.75-in.) chord and a constant 7% thickness. These vanes are set at their design stagger (minimum loss incidence) and the inlet guide vanes fixed in an unclocked position; that is, the IGV and stator vane stacking axis locations circumferentially coincide. The IGV–rotor and rotor–stator midspan axial spacings are 41.4% and 39.0% chord, respectively.

Data Acquisition and Analysis

Forcing Function and Inlet Guide Vane Response

The rotor-generated unsteady aerodynamic forcing function and the resultant IGV steady and unsteady surface pressure distributions are measured at 90% span, Fig. 4. An unsteady static-pressure probe is utilized to determine the potential flow–generated forcing function upstream of the rotor. To minimize interference effects,

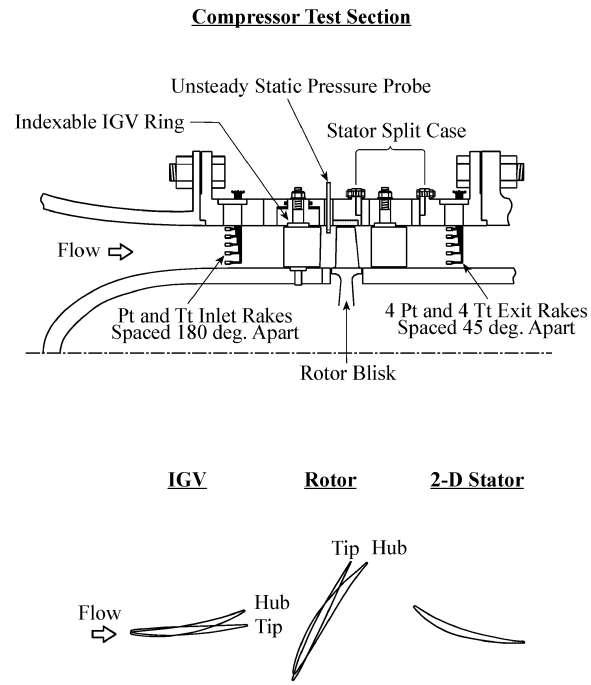

Fig. 3 Purdue transonic research compressor.

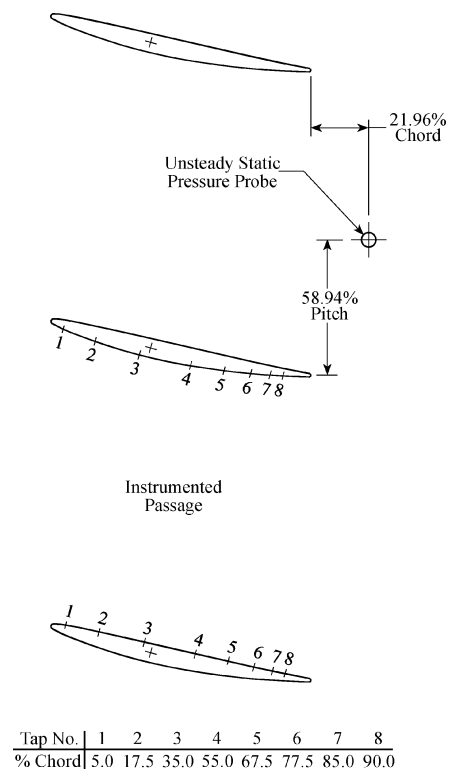

Tap No.	1	2	3	4	5	6	7	8
% Chord	5.0	17.5	35.0	55.0	67.5	77.5	85.0	90.0

Fig. 4 IGV 90% span instrumentation.

it is located 21.96% chord downstream and circumferentially positioned 58.94% pitch above the IGV trailing edge. Measurements of the resultant IGV unsteady response are obtained with vane-mounted high-response Kulite 5-psi sealed gauge pressure transducers reverse-mounted within the suction surface of one vane and the pressure surface of an adjacent vane. A second set of vanes instrumented with static pressure taps at these same locations are used to acquire the steady surface pressure distributions.

Unsteady pressures exceeding the quoted linear range of the transducers are measured. Hence, the transducers were statically calibrated over a pressure range from 0 to 7 psi. Accounting for nonlinearities, the unsteady pressure measurement maximum uncertainty

is estimated to be 0.5%, with the frequency responses estimated to be 50 and 70 kHz for the unsteady static pressure probe and instrumented vanes.

The bridge voltage to the pressure transducers is provided by a Syminex 24-channel signal conditioning unit, with the signals conditioned by high-bandwidth ac-coupled amplifiers. The instantaneous signals are simultaneously recorded along with a once-per-rev pulse from a shaft-mounted optical sensor on analog tape. Approximately 20,000 revolutions of data are recorded with an 80-kHz recorder frequency response at a tape speed of 76.2 cm/s (30 in./s).

The data are processed off-line and phase-lock averaged over 500 revolutions. The signals are digitized at a rate of 1 MHz and stored to disk, with the once-per-revolution signal used as the data initiation pulse and the number of samples chosen to encompass one rotor revolution. Prior to analysis, the phase-lock averaged waveforms are shifted in the time domain to represent the time-variant flow field for a reference passage, with the lower vane response data further shifted to the upper vane in this passage. The forcing function data therefore lag the reference vane trailing edge unsteady surface pressure measurements by 43.3% of a blade-pass period.

Particle Image Velocimetry

To characterize the rotor–IGV interactions, instantaneous IGV passage flow field data are obtained over a rotor blade-pass period using particle image velocimetry (PIV). PIV is a whole field measurement technique providing quantitative flow visualization of the velocity field within a two-dimensional measurement plane. The flow is seeded with tracer particles and the vane-to-vane plane of interest illuminated with a light sheet generated by the timed double pulse of a high-powered laser. A charge-coupled device (CCD) camera synchronized to the laser records light scattered by the seed particles within this plane. Images captured for each pulse of the laser are divided into interrogation regions and a fast Fourier transform (FFT)-based correlation algorithm is used to determine the average distance traveled by particle pairs within the regions. Velocity vectors are then computed by dividing each displacement vector by the time between laser pulses. Interrogation regions 32×32 pixels in size with a 50% overlap are used in the current study, yielding a maximum of 3844 velocity vectors per image.

The DANTEC PIV system utilized in these experiments consists of three main components: a NewWave Research Minilase III Nd:YAG laser, a Roper Scientific Megaplus ES1.0 digital camera, and a dedicated PIV 2100 processor. The 30-mJ laser emits pulses of green light (532 nm) 5–7 ns in duration from its dual heads at a rate of 15 Hz, with the variable time between laser head pulses specified in the PIV software. When operated in cross-correlation mode, separate images for the two successive laser pulses are recorded on the digital camera's 1008×1018 pixel CCD array. The dedicated PIV 2100 processor provides near real-time vector processing of these images using an FFT correlation technique, with particle displacements resolved to within 1/10 of a pixel through a subpixel interpolation routine. This component is also responsible for the synchronization of the laser, camera, and additional external timing signals. DANTEC FlowManager software is used to perform off-line validation and postprocessing, with directional velocity information unambiguously determined because the initial and final particle positions are recorded in separate images.

Measurement of the unsteady flowfield in various instances over one rotor blade-pass period are obtained using the output of a phase delay generator to externally trigger the PIV acquisition. Time delays are calculated for a series of desired rotor angular positions relative to the stationary vanes based on the measured rotor speed. These delays are then set on the LaserStrobe 165 phase delay generator, which is capable of accurately delaying the rotor shaft once-per-revolution input signal up to 999.9 μs in 0.1-μs intervals.

The 90% span IGV flowfield is illuminated by a 1-mm-thick light sheet introduced upstream through the inlet using a combination of cylindrical and spherical lenses. Images of the seeded vane-to-vane flow field are acquired through a removable constant-thickness (1.0 in.) Plexiglas window contoured to the flowpath outer diameter. The lens magnification factor is determined by imaging a calibration grid within the passage at 90% span. Optical distortion caused by the window curvature is accounted for using separate horizontal and vertical scale factors.

Seed particles small enough to accurately track the flow and large enough to scatter sufficient light to be detected with the imaging system are generated by a Rosco 1600 fog machine. A high volume of seed particles are produced by discharging a heated and pressurized glycol-based mixture into the atmosphere, where it immediately vaporizes and then condenses into a fine mist of monodisperse particles. Uniform seed density within the test section is achieved by introducing these particles upstream of the bell-mouth inlet and allowing them to disperse into the ambient air prior to being drawn through the facility.

Results

The transonic compressor IGVs were restaggered 15.75 deg in the direction of rotor rotation from design stagger for this off-design investigation, nearly aligning the vane exit metal angle with the detached rotor shocks under transonic operating conditions. The required transonic rotor inlet flowfield is achieved with an open throttle setting and a corrected speed of 22,050 rpm. Data are acquired for this transonic operating condition and a subsonic operating condition, $N_c = 20{,}000$ rpm.

Rotor-Generated Forcing Function

Rotor-generated unsteady static pressure field data are presented in Fig. 5. The static pressure perturbation is nondimensionalized by the inlet total pressure, time is nondimensionalized by blade-pass period, and only 5 of the 19 blade-pass periods in a revolution are shown. The spectral content of the phase-lock averaged forcing functions, computed using an FFT algorithm over a data window encompassing one rotor revolution, is shown in Fig. 6.

The static pressure fluctuations under subsonic operating conditions are essentially sinusoidal, reaching a maximum $p_s/P_{t,\mathrm{in}}$ value of 0.15. At 22,050 rpm, the rotor relative velocity is transonic, demonstrated by the impulsive static pressure rise corresponding to the passing of rotor leading edge shocks. This impulsive peak-to-peak amplitude is only slightly larger than that at $N_c = 20{,}000$ rpm.

The first harmonic dominates the frequency spectrum at $N_c = 20{,}000$ rpm, with the second and third harmonics nearly equal, but considerably smaller. In contrast, the frequency data at $N_c = 22{,}050$ rpm reveal a relatively large contribution of higher harmonics. Thus, the first five blade-pass harmonics are needed to

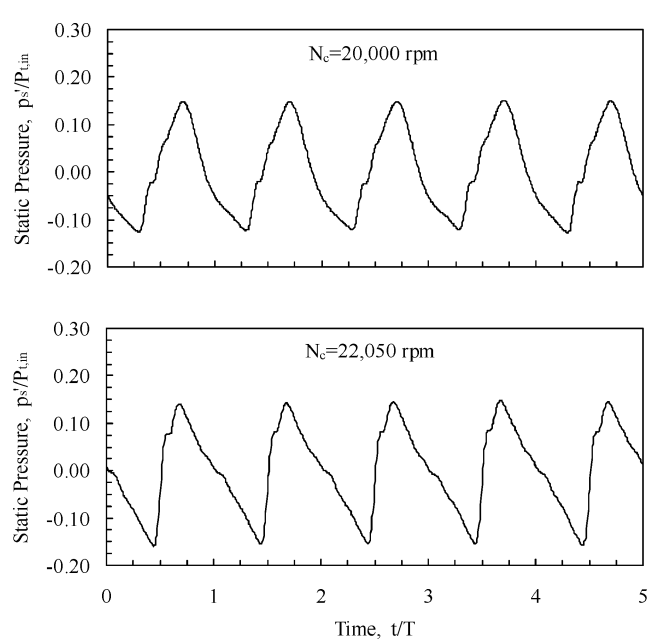

Fig. 5 Rotor-generated forcing function to IGVs.

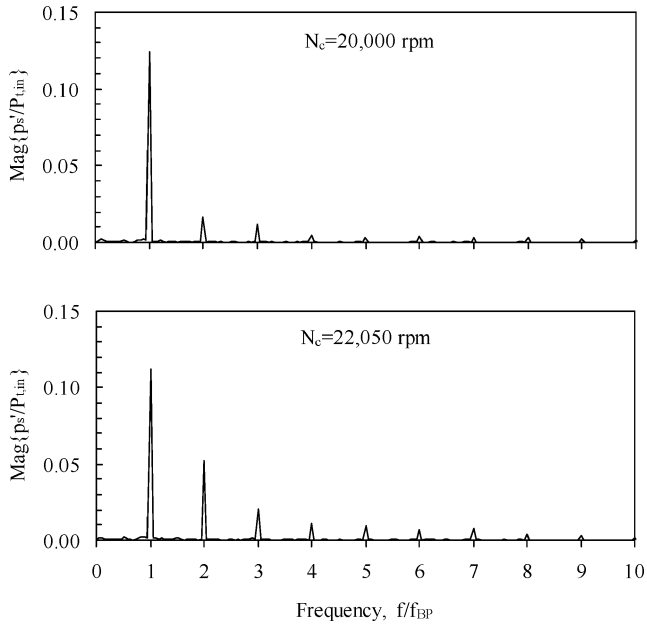

Fig. 6 Forcing function harmonic content.

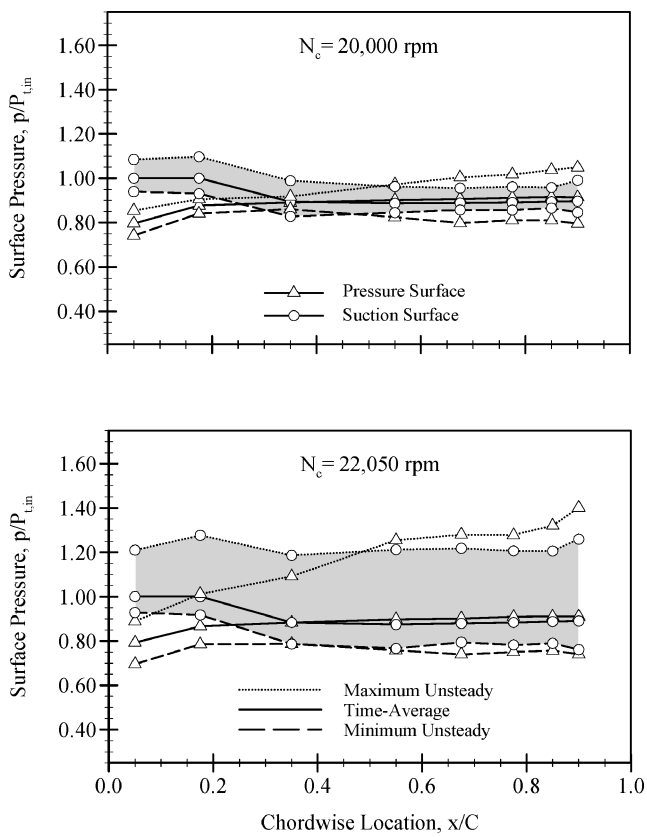

Fig. 7 IGV unsteady pressure envelopes.

accurately describe this forcing function, whereas only three are required under subsonic operating conditions.

Inlet Guide Vane Unsteady Aerodynamic Response

IGV unsteady pressure envelopes, the minimum and maximum unsteady pressures in the time-variant IGV response at each chordwise location, are presented together with the respective time-averaged surface pressure distributions in Fig. 7.

The time-averaged pressure distributions indicate a high-pressure region associated with the presence of a stagnation point on the IGV suction surface under both operating conditions. The pressure surface data reveal a low-pressure area at the leading edge that decreases as the corrected speed is increased.

The unsteady surface pressure amplitudes are smallest at 20,000 rpm. After reaching a maximum at 17.5% chord, the suction surface unsteadiness decreases smoothly to approximately 10% $P_{t,\mathrm{in}}$ near 65% chord. Over the remainder of the surface, the unsteadiness is relatively constant except near the trailing edge, where the pressure fluctuations are nearly equal to those at the leading edge. The vane pressure surface unsteadiness decreases over the leading 35% chord, with the unsteady pressure envelope increasing significantly to a maximum of 25.3% $P_{t,\mathrm{in}}$ near the trailing edge.

The IGV response to the rotor leading edge shocks at $N_c = 22{,}050$ rpm is dramatic, with unsteady loading greater than 40% of the inlet total pressure over the majority of both vane surfaces. The suction surface envelope increases between the leading edge and 35% chord, with the static pressure fluctuations then remaining relatively constant. An increase in the trailing edge region, similar to that at 20,000 rpm, raises the unsteadiness to almost 50% of the inlet total pressure. In contrast, the pressure surface unsteadiness sharply rises near the leading edge to 55% chord and continues to increase to a maximum of 66% $P_{t,\mathrm{in}}$ in the trailing edge region. This maximum, although occurring at the same location, is 2.6 times larger than that at $N_c = 20{,}000$ rpm, with the forcing function peak-to-peak static pressure perturbation only 1.1 times larger.

Inlet Guide Vane Response and Spectral Analysis

The time-variant surface pressures from which the unsteady pressure envelopes are constructed are presented, with only 5 of the 19 blade-pass periods shown for clarity. These ac-coupled waveforms represent a phase-lock average of 500 rotor revolutions, with pressure and time normalized by the inlet total pressure and blade-pass period, respectively. The frequency spectra are computed using an FFT algorithm over a window encompassing a complete rotor revolution of ensemble-averaged unsteady pressure data.

A flat unsteady pressure profile on the vane pressure surface follows a comparatively large leading edge unsteadiness under subsonic operating conditions (Fig. 8). The remaining surface

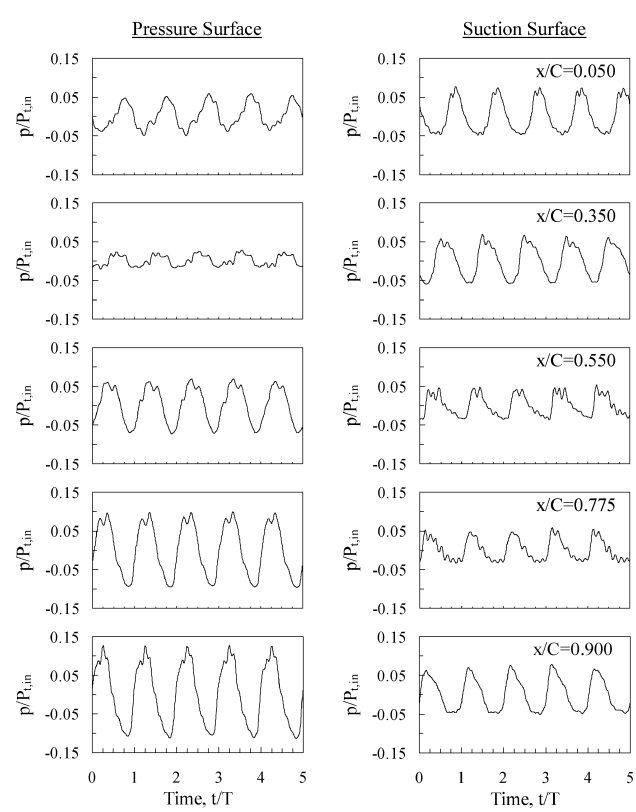

Fig. 8 Unsteady surface pressures—20,000 rpm.

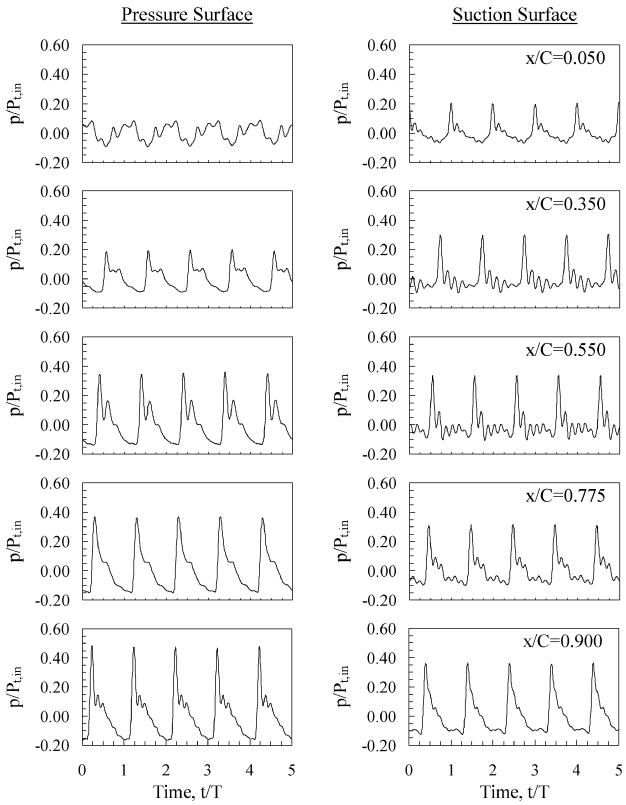

Fig. 9 Unsteady surface pressures—22,050 rpm.

pressures are predominately sinusoidal, with a minor deficit present at or near the waveform peak. As evidenced in the unsteady pressure envelopes, the waveform peak-to-peak amplitude increases from a minimum at $x/C = 0.35$ to a maximum at the trailing edge. Note that the waveform at the suction surface leading edge possesses characteristics similar to the majority of the pressure surface data. Aft of this location, the suction surface waveforms transition from sinusoidal to sawtooth, with peak-to-peak amplitudes generally decreasing toward the trailing edge. An upstream propagating wave phenomenon is present, most notably on the suction surface ahead of midspan.

The vane static surface pressures are markedly different at 22,050 rpm, where the rotor relative flow field is transonic. The IGV response to the rotor leading edge shocks is impulsive at a majority of the measurement locations, with peak amplitudes at the pressure surface trailing edge approaching 50% of the inlet total pressure, Fig. 9. The impulse on the pressure surface is apparent to 35% chord as the amplitudes decay upstream of the trailing edge. Note that the leading edge unsteadiness is relatively small but significant, being nearly as large as that at the pressure surface trailing edge for $N_c = 20{,}000$ rpm. The pressure and suction surface trailing edge waveforms are similar, though the suction surface waveform is smaller in amplitude and the sharp pressure rise occurs later in the blade-pass period because of the shock first being cut by the pressure surface. Upstream of the trailing edge, the amplitudes remain relatively constant from 75% to 35% chord and higher blade-pass harmonics are observed. An upstream propagating wave is again evident on both vane surfaces, because the waveform peaks occur later in time as one moves forward from the trailing to leading edge.

Harmonics greater than four times blade-pass frequency make no contribution to the IGV unsteady aerodynamics at $N_c = 20{,}000$ rpm, Fig. 10. The pressure surface data show a gradual decrease in the dominant first harmonic from the trailing edge to midchord and a sharp decrease from 55% to 35% chord. At the leading edge, the first harmonic has increased to 4.1% of the inlet total pressure. On the suction surface, the first harmonic generally increases from 75% to 35% chord, with the leading and trailing edge amplitudes 5.6% and 5.2% of the inlet total pressure.

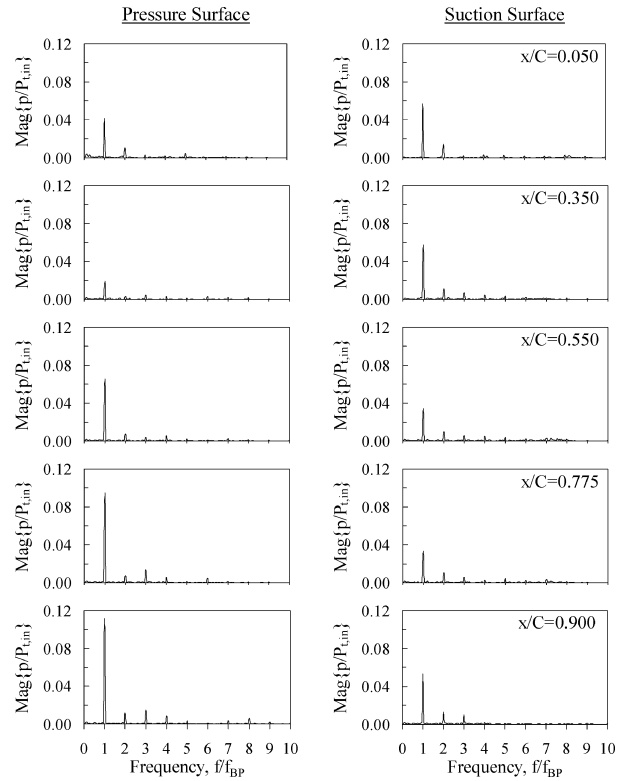

Fig. 10 IGV response harmonics—20,000 rpm.

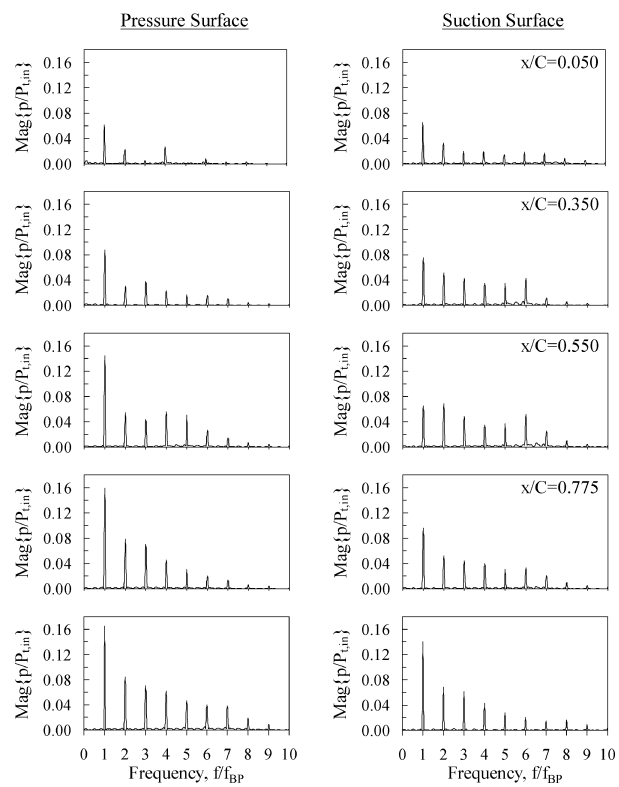

Fig. 11 IGV response harmonics—22,050 rpm.

A significant increase in the higher harmonics under transonic operating conditions is evident (Fig. 11). The frequency spectra for both surfaces indicate that the harmonic amplitude tends to decrease linearly with frequency, not exponentially like the corresponding forcing function data. Harmonic amplitudes on the pressure surface generally decrease upstream of the trailing edge, where the first harmonic is 16.4% of the inlet total pressure. The pressure and suction surface trailing edge spectra are very similar except

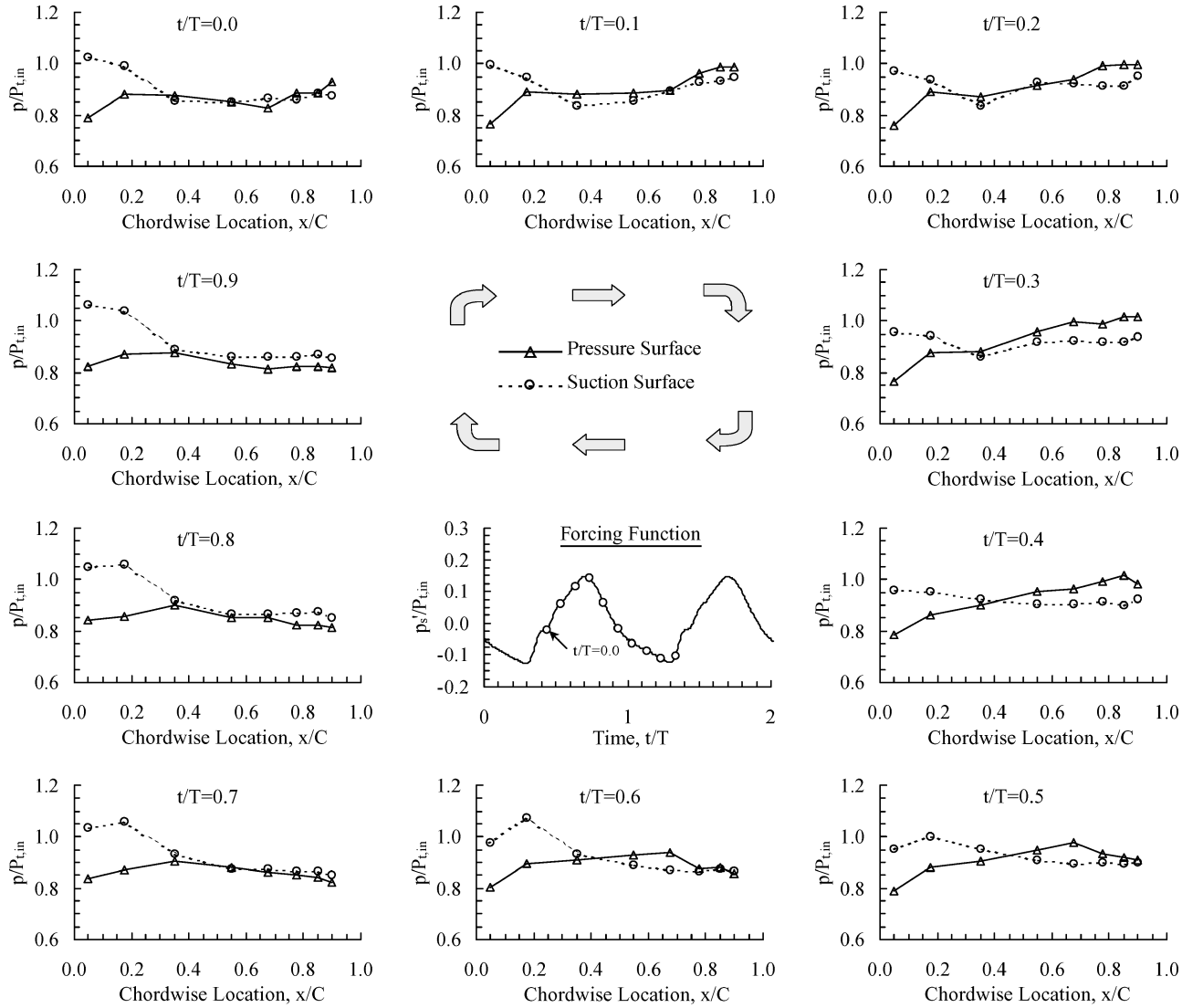

Fig. 12 Time-variant IGV loading—20,000 rpm.

for the latter's slightly smaller amplitude. Upstream of the suction surface trailing edge, the first harmonic decreases to 55% chord, where it is nearly equal to the second harmonic. Ahead of this location, the first harmonic magnitude increases slightly, with as many as seven harmonics present in the leading edge region.

Time-Variant Surface Pressures

IGV surface pressures at several time instances provide insight into the upstream propagating wave phenomena. The surface pressures are presented for 10 equally spaced time increments over one rotor blade-pass period along with the rotor-generated unsteady static pressure field. Recall that the forcing function data were not shifted to the reference vane trailing edge and therefore lag the surface pressure measurements by 43.3% of a blade-pass period. For reference, symbols on the forcing function correspond to the time at which the surface pressure data are acquired.

An upstream propagating wave phenomenon is evident in the time-variant pressure distributions at $N_c = 20{,}000$ rpm as the IGVs smoothly respond to the unsteady rotor-generated potential field, Fig. 12. The pressure surface trailing edge static pressure gradually increases between $t/T = 0.8$ and 0.3. This static pressure peak migrates toward the leading edge as the interaction cycle progresses. The suction surface fluctuations are small aft of midchord, with leading edge region unsteadiness dominate over the cycle.

The time-variant pressure data for the transonic operating condition, Fig. 13, also indicate an upstream propagating phenomenon. A response is first observed on the pressure surface trailing edge at $t/T = 0.2$. This significant static pressure rise results from the impact of a rotor leading edge shock and the subsequent reflection generated at the vane surface. Note that a time lag exists between the forcing function and vane response because the trailing edge unsteady pressure tap is 32% chord upstream of the unsteady static pressure probe.

At $t/T = 0.3$, the shock and reflection have progressed upstream, with a sharp static pressure decrease aft of a maximum value of 130% $P_{t,\mathrm{in}}$ at 85% chord. The suction surface static pressure rise indicates that the incident shock has diffracted around the vane trailing edge at $t/T = 0.4$. The suction surface trailing edge unsteadiness is approximately equal to the maximum pressure surface fluctuation, which has migrated upstream to 67.5% chord. A noticeable decrease in the pressure surface unsteadiness occurs at the next time instance, with higher suction surface static pressures over the majority of the vane chord. The suction surface unsteadiness grows as it travels toward the leading edge, reaching a maximum at $t/T = 0.0$. Pressure surface fluctuations are minimal at these later times, a result of decreased shock strength as energy is dissipated during its interaction with the upstream vane row. Additionally, the pressure and suction surface trailing edge pressure distributions are nearly identical for the remainder of the cycle up to $t/T = 0.1$.

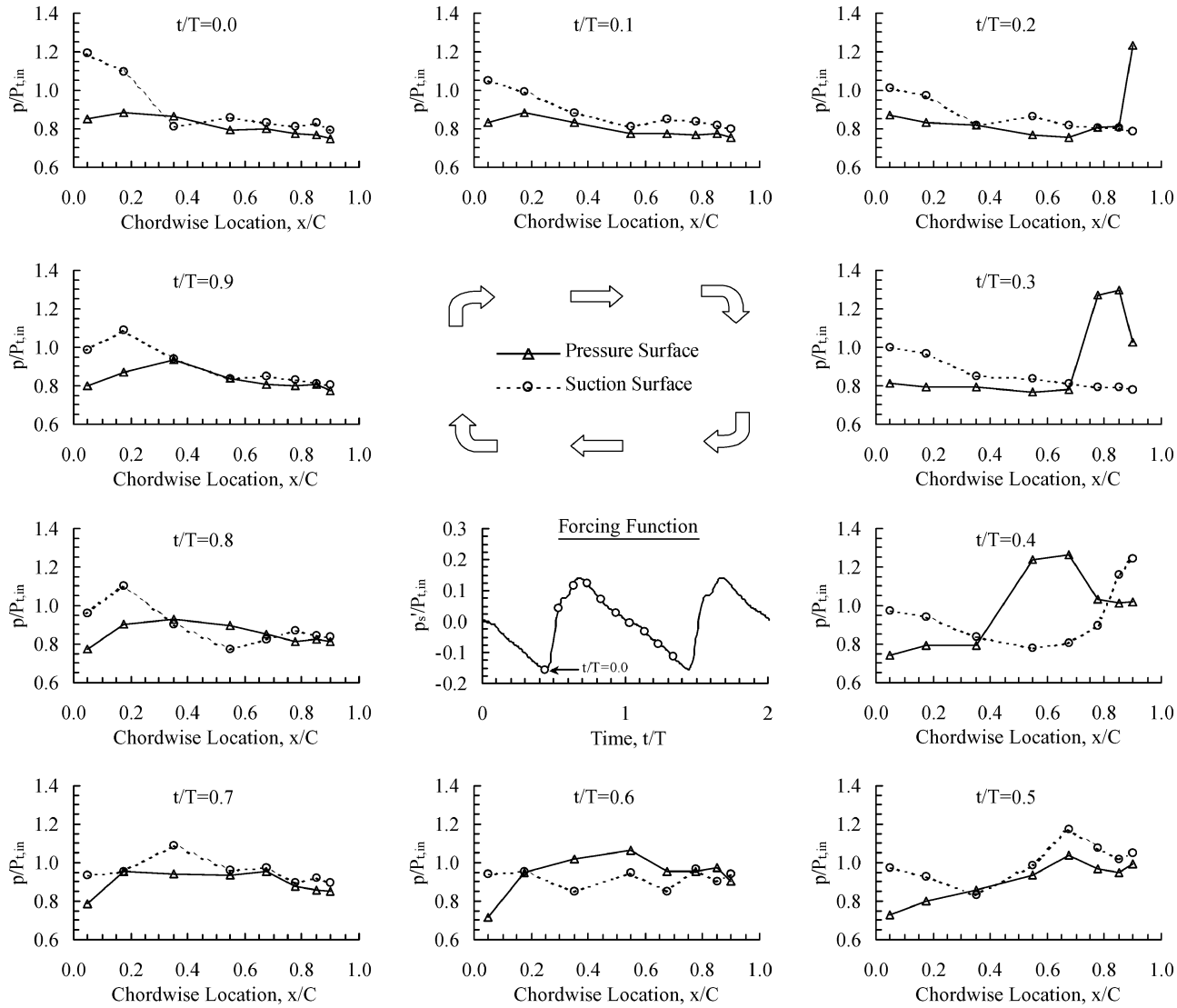

Fig. 13 Time-variant IGV loading—22,050 rpm.

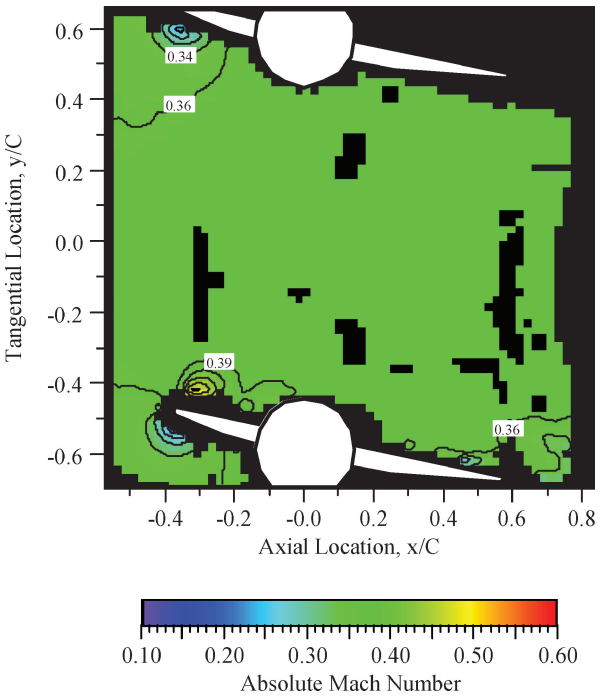

Fig. 14 Time-averaged vane-to-vane flowfield—20,000 rpm.

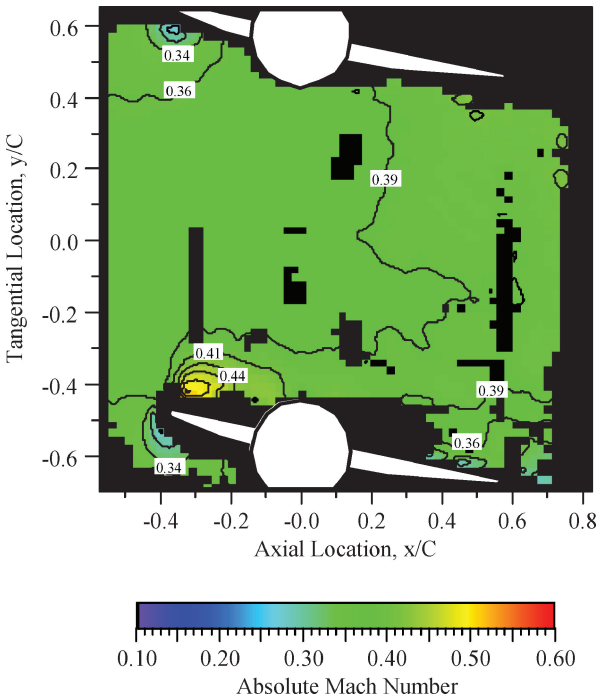

Fig. 15 Time-averaged vane-to-vane flowfield—22,050 rpm.

Inlet Guide Vane to Inlet Guide Vane Passage Flowfield

PIV measurements of the unsteady vane-to-vane flowfield at 90% span are obtained at 10 equally spaced time intervals over one blade-pass period, with the data at each time instant representing an ensemble average of 32 instantaneous vector fields. Note that areas exist within the flowfield where valid data, a minimum of 10 vectors at a given interrogation region within the ensemble, were not acquired. Time-average flowfields are computed from an arithmetic average of these time-variant measurements over a complete blade-pass period.

The passage time-average absolute Mach numbers, Figs. 14–15, show that the subsonic and transonic flowfields are very similar. These data are in excellent agreement with the compressor inlet Mach numbers, 0.34 and 0.35, and the vane steady surface pressure data, which indicated an area of high pressure on the suction surface leading edge associated with a stagnation point at both operating conditions. This correlates well with the suction surface low-velocity region in the steady absolute Mach number results. On the pressure surface, the steady pressure and the PIV data both show a low-pressure, high-velocity region at the leading edge.

The time-variant absolute Mach number data under subsonic operating conditions, Fig. 16, closely resemble the time-average flowfield. A low-velocity region beyond the pressure surface trailing edge is apparent for $t/T = 0.1$–0.4 as the passage flow smoothly responds to the unsteady backpressure associated with the rotor potential field. Reductions in the vane leading edge Mach number at later instances in the blade-pass period are observed as the potential field's effect reaches deeper into the vane passage.

In contrast, complex rotor–IGV interactions are revealed in the time-variant absolute Mach number results for the transonic operating condition, Fig. 17. A rotor leading edge shock is first cut by the upper vane pressure surface and diffracted around the trailing edge at $t/T = 0.2$, with the diffracted shock segment clearly evident on the suction surface at the next time instant. This shock weakens slightly as it progresses upstream, moving closer to the lower vane pressure surface. At $t/T = 0.6$, a process has begun which splits the shock into two segments near mid-passage 0.3

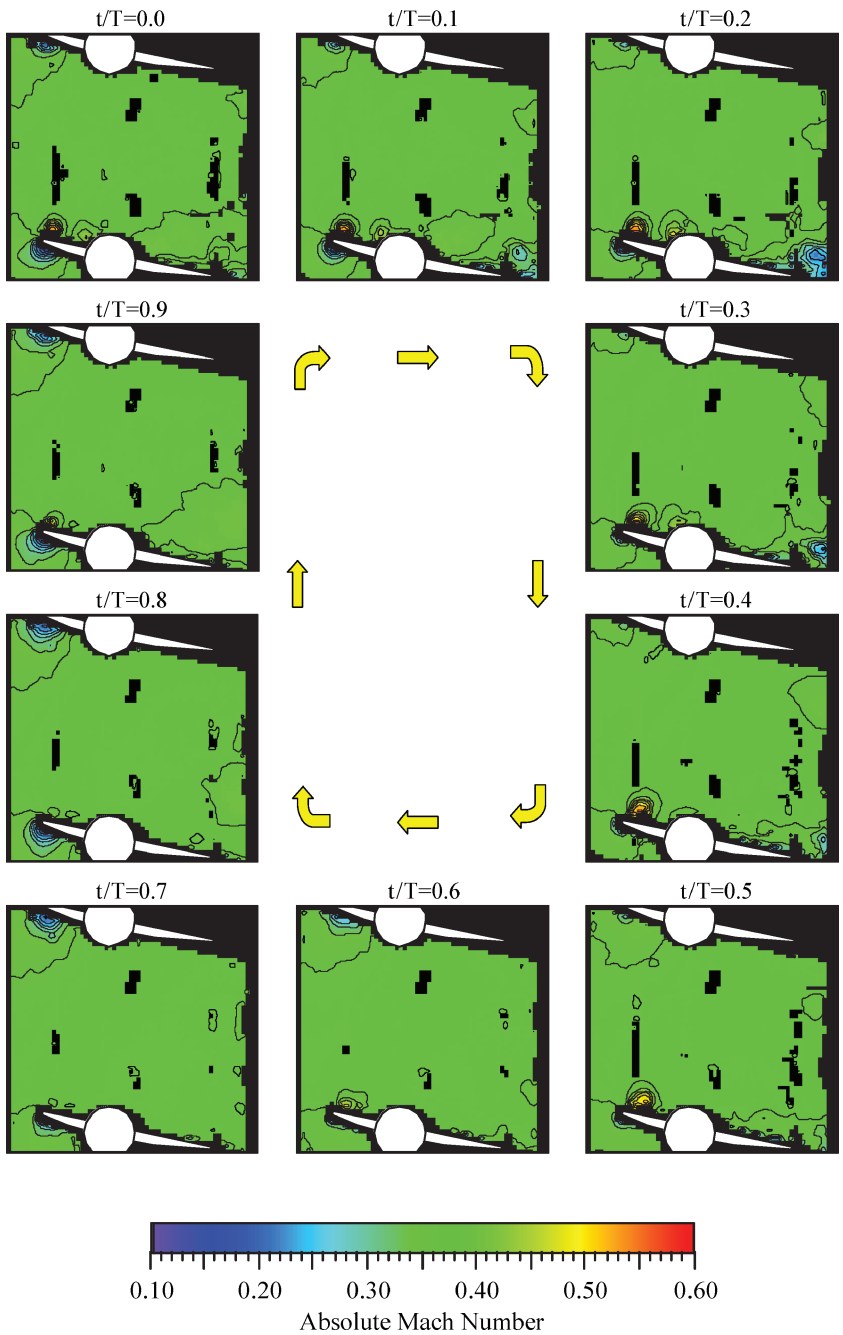

Fig. 16 Time-variant absolute Mach number—20,000 rpm.

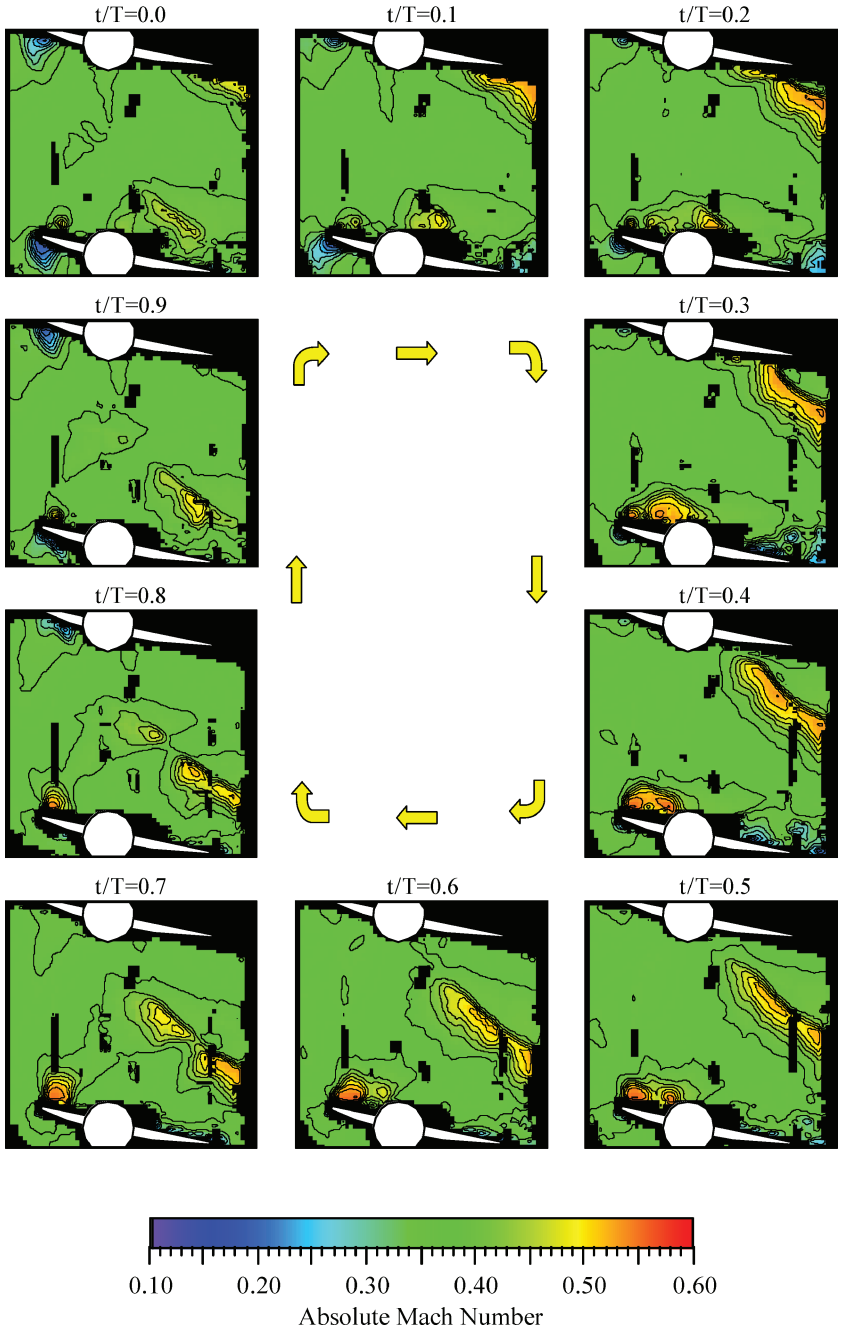

Fig. 17 Time-variant IGV absolute Mach number—22,050 rpm.

blade-pass periods later. The weaker of the two segments decays rapidly, whereas the remaining shock segment continues toward the lower vane pressure surface. This segment impacts the pressure surface between $t/T = 0.1$ and $t/T = 0.2$ and a resultant reflection from the surface forms, as indicated by the low-velocity region behind the shock. As the shock and reflection travel upstream, the high-velocity region ahead of the shock merges with a leading edge high-velocity region of nearly equal magnitude at $t/T = 0.3$. This high-velocity region decays with time, encompassing a majority of the leading edge to $t/T = 0.6$ and reaching a minimum at $t/T = 0.0$. As this high-velocity region weakens, a corresponding low-velocity region grows on the pressure surface leading edge, and vice versa, throughout the rotor–IGV interaction cycle.

The spatial periodicity of the unsteady flow field is also demonstrated in Fig. 17, with this periodicity set by the unequal blade-vane count. This is best illustrated at $t/T = 0.0$ where two shock segments are visible in the passage, one near the lower vane pressure surface and the other just below the upper vane trailing edge. The data correctly show that the circumferential distance between adjacent rotor leading edge shocks is slightly smaller than that of the IGVs, a consequence of the compressor having 18 IGVs and 19 rotor blades. Thus, interactions on the upper vane lead those on the lower vane by an interblade phase of 380 deg, with any given rotor blade requiring 1.06 blade-pass periods to traverse an IGV passage.

The complex rotor–IGV interactions are readily identifiable in the time-variant tangential Mach number results, Fig. 18. Recall that with an oblique shock, the flow is deflected toward the shock, a result of the normal velocity component decreasing and the tangential velocity component remaining constant across the discontinuity. The data confirm that a rotor shock segment impacts the lower vane pressure surface between $t/T = 0.1$ and $t/T = 0.2$, with the shock from an adjacent rotor blade cut by the trailing edge of the upper

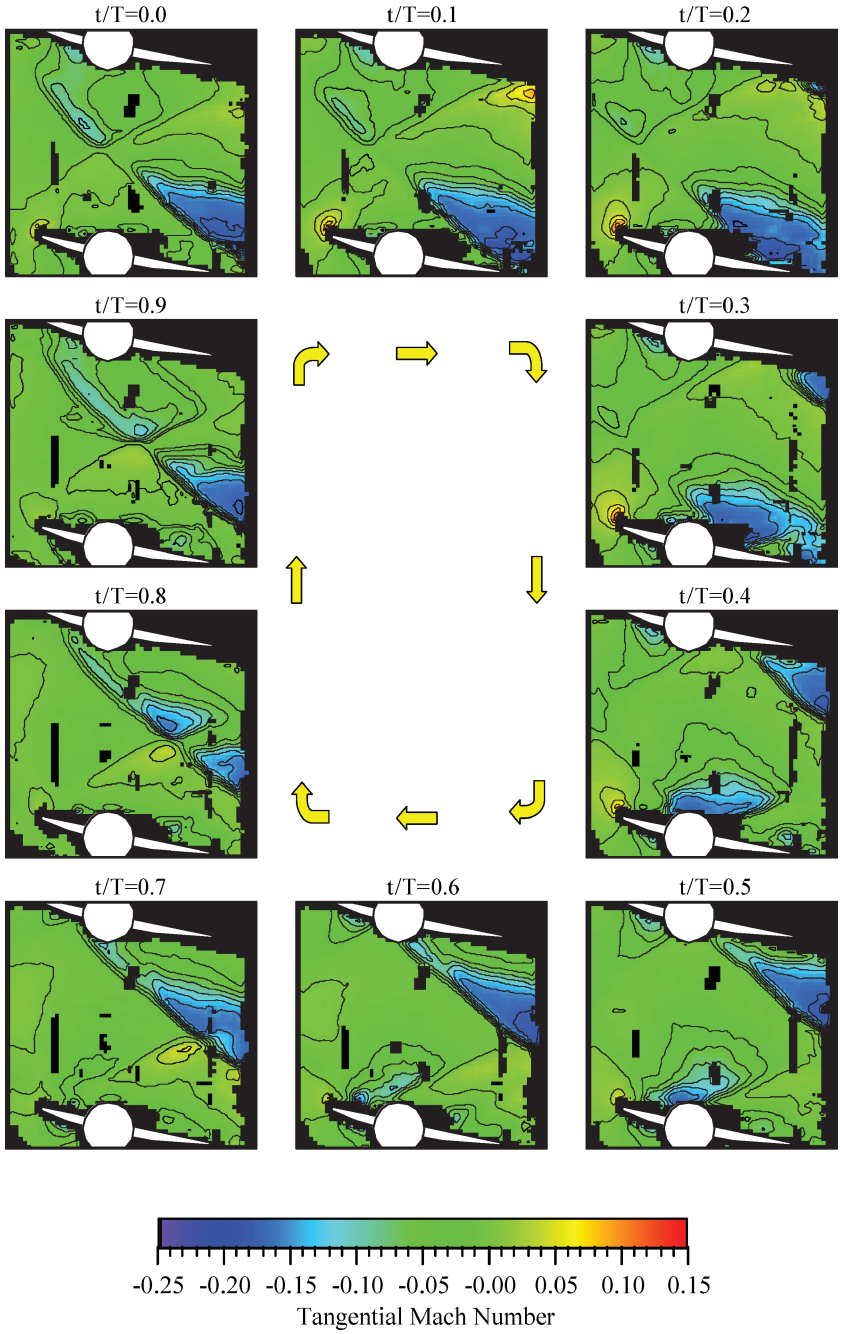

Fig. 18 Time-variant IGV tangential Mach number—22,050 rpm.

vane at the later time. Also visible at $t/T = 0.2$ is a reflection generated behind the incident shock to satisfy the vane surface boundary condition. This shock reflection is relatively weak, a consequence of the oblique shock deflecting the fluid stream in the same direction as the vane stagger. The reflection is more prevalent at the next time instant where it bisects the incident shock segment at approximately 80% chord.

As the cycle progresses, the reflection moves toward midpassage while the shock travels upstream along the vane surface, reaching the leading edge at $t/T = 0.7$. The reflection and shock from the adjacent rotor blade intersect at this time, with the reflection passing completely through the shock and forming an X pattern near midpassage 0.2 blade-pass periods later. After the rotor leading edge shock is bisected, both segments continue to move along their original trajectory upstream toward the lower vane leading edge. The weaker of the two segments decays, exiting the passage prior to $t/T = 0.5$, and the rotor–IGV interaction cycle repeats as the remaining segment impacts the lower vane pressure surface slightly after $t/T = 0.1$.

Time-Variant Leading and Trailing Edge Flow Fields

PIV data were also acquired near the leading and trailing edges of the lower vane in the reference passage at $N_c = 22{,}050$ rpm. Steep tangential Mach number gradients, Fig. 19, indicate the presence of an oblique shock near the vane trailing edge at $t/T = 0.0$. Recall that the flow is deflected toward the shock after passing through the discontinuity. This shock segment impacts the vane pressure surface prior to $t/T = 0.2$ per the corresponding passage data. Upon impact, a reflection from the surface is generated to satisfy the boundary condition, with this reflection relatively weak as the oblique shock turns the flow in the direction of the vane stagger. This reflection grows significantly between $t/T = 0.2$ and $t/T = 0.3$, bisecting the incident shock segment at the later time. Also evident at this instant is a suction surface reflection generated by a previous rotor

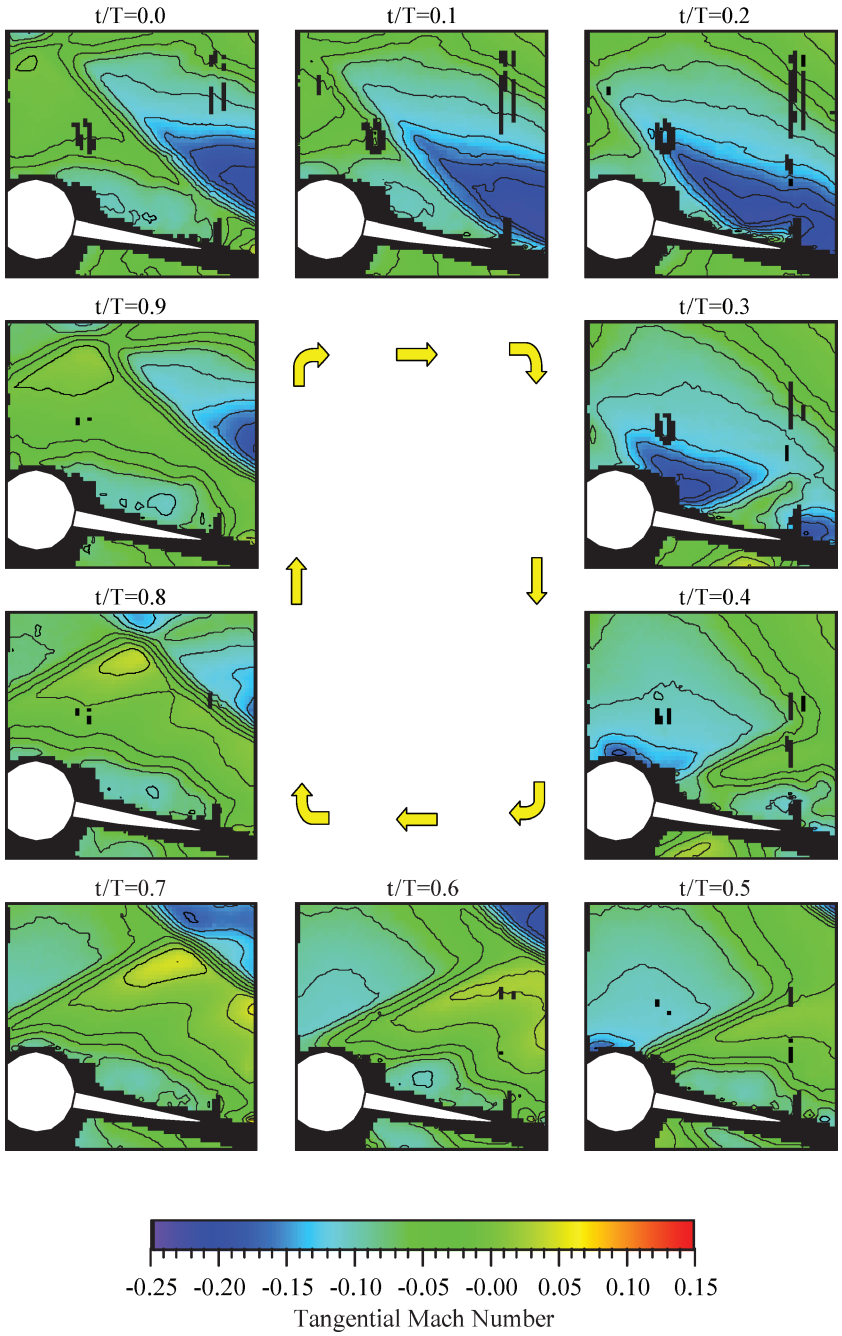

Fig. 19 Time-variant IGV trailing edge tangential Mach number—22,050 rpm.

leading shock which has traversed the adjacent passage. The suction surface reflection lags the pressure surface reflection as they proceed upstream, with the suction surface reflection leaving the measurement region at $t/T = 0.5$. On the pressure surface, the shock diminishes and the reflection migrates deeper into the passage as time progresses. At $t/T = 0.6$ the reflection and shock from the next rotor blade intersect, resulting in the two shock segments 0.3 blade-pass periods later. The flow near the trailing edge surface is smoothly turned by the vane in the absence of the shock and its reflection.

Time-variant leading edge tangential Mach number data are presented in Fig. 20. The data confirm an interaction between the reflection and shock from an adjacent rotor blade near midpassage at $t/T = 0.9$, with a portion of the shock continuing toward the vane pressure surface as time progresses. As this shock segment traverses upstream, flow around the leading edge to the pressure surface is reduced. Note the reflection generated on the pressure surface first observed at $t/T = 0.4$ reaches the leading edge 0.5 blade-pass periods later and is responsible for the tangential Mach number being a minimum at this instant.

Unsteady Lift

Unsteady lift for the off-design operating conditions of these experiments and the near-peak-efficiency condition are shown in Fig. 21. Plotted are four harmonic amplitudes of the unsteady lift normalized by the inlet total pressure and vane chord. The first harmonic is dominant, with the transonic off-design first harmonic magnitude 44.5% greater than that for the near peak efficiency condition. Also, the higher harmonic amplitudes at the off-design point are greater than 120% of their near peak efficiency counterparts. The subsonic off-design first harmonic amplitude is slightly less than that for the transonic off-design case, with only minor higher harmonic contributions because of the subsonic rotor flow field.

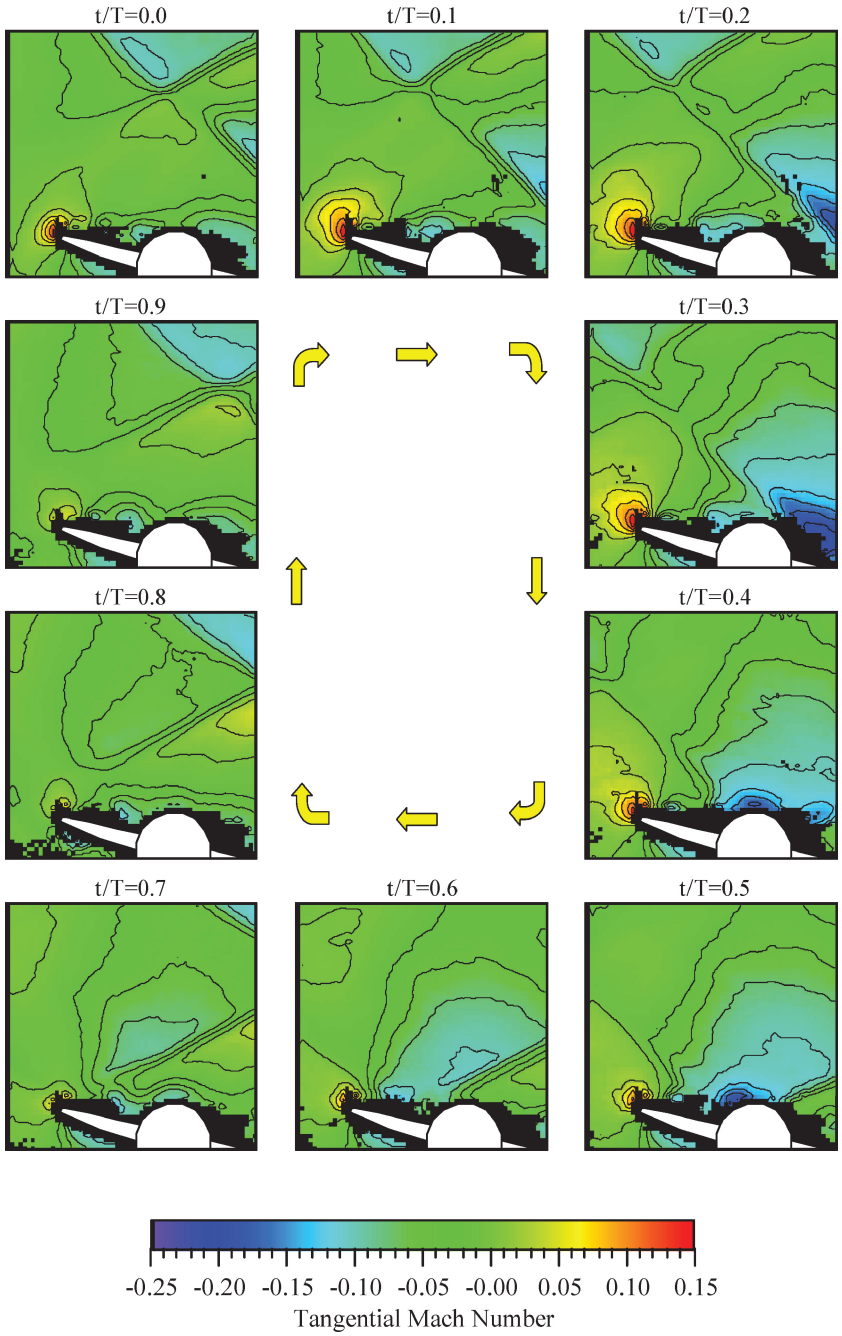

Fig. 20 Time-variant IGV leading edge tangential Mach number—22,050 rpm.

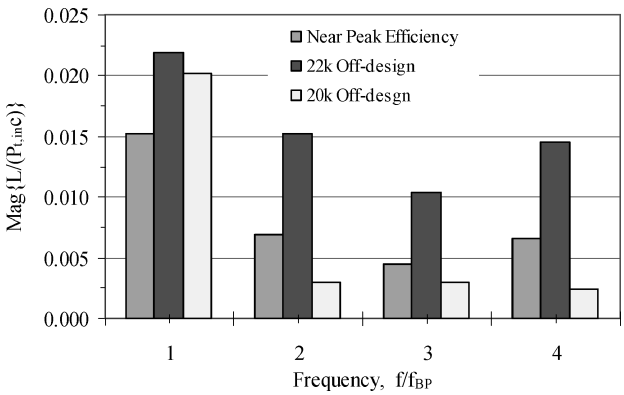

Fig. 21 Unsteady lift harmonic amplitudes.

Summary

Detailed unsteady aerodynamic rotor–IGV interaction data were acquired under off-design operating conditions in a research $1\frac{1}{2}$-stage compressor. Specifically, the IGVs were restaggered to nearly align the vane exit metal angle with detached rotor shocks at the transonic operating condition, resulting in the maximum modal force excitation to the IGVs.

The rotor-generated unsteady static-pressure field data showed that the peak-to-peak fluctuations under transonic operating conditions were only slightly larger than those under subsonic conditions. However, the $N_c = 22{,}050$ rpm data contained an impulsive static pressure rise due to the rotor leading edge shocks.

The steady surface pressures and time-averaged passage flowfields were very similar, with the passage absolute Mach numbers scaling with rotor speed. In contrast, there were significant differences in the subsonic and transonic rotor time-variant unsteady

aerodynamics. There was a substantial increase in the unsteady surface pressure envelope at $N_c = 22{,}050$ rpm, with a maximum pressure surface fluctuation 2.6 times larger than that at 20,000 rpm. The corresponding forcing function peak-to-peak amplitude was only 1.1 times larger at the transonic operating condition.

Upstream propagating wave phenomena at both rotor operating conditions were confirmed by the time-variant pressure distributions. The surface pressure data at $N_c = 20{,}000$ rpm showed that the IGVs smoothly responded to the rotor-generated potential field. In contrast, there were large static pressure increases on the vane surfaces at the transonic operating condition because of the incident shocks.

The unsteady absolute Mach number data at $N_c = 20{,}000$ rpm closely resembled the time-average flowfield. At $N_c = 22{,}050$ rpm, the PIV data showed complex rotor–IGV interactions. Rotor leading edge shocks impact the IGV pressure surface trailing edge, where a relatively weak reflection is generated. An interaction between the reflection and shock from an adjacent rotor blade occurs midway through the cycle and results in the bisection of the incident shock. The weaker of the two segments exits the passage and the other continues migrating toward the vane pressure surface, beginning the next interaction cycle.

The first harmonic unsteady lift at the transonic off-design operating point was 44.5% greater than that at near peak efficiency, thereby confirming that the highest strains occur when the reset angle causes the rotor to be on the verge of becoming transonic and the vane exit metal angle is aligned with the rotor shocks.

Acknowledgment

This research was sponsored, in part, by the Air Force Office of Scientific Research (AFOSR). This support is most gratefully acknowledged.

References

[1]Sanders, A. J., and Fleeter, S., "Experimental Investigation of Rotor–Inlet Guide Vane Interactions in a Transonic Axial-Flow Compressor," *Journal of Propulsion and Power*, Vol. 106, No. 3, 2000, pp. 421–430.

[2]Sanders, A. J., Papalia, J., and Fleeter, S., "A PIV Investigation of Rotor–IGV Interactions in a Transonic Axial-Flow Compressor," *Journal of Propulsion and Power*, Vol. 18, No. 5, 2002, pp. 969–977.

[3]Richman, M., and Fleeter, S., "Nonlinear Turbo/TurboAE Simulation of Transonic IGV–Rotor Interactions," *International Journal of Rotating Machinery*, Vol. 8, No. 4, 2002, pp. 259–274.

[4]Gottfried, D., and Fleeter, S., "Turbomachine Blade Row Interaction Predictions with A Three-Dimensional Finite Element Method," *Journal of Propulsion and Power*, Vol. 18, No. 5, 2002, pp. 978–989.

[5]Silkowski, P. D., Rhie, C. M., Copeland, G. S., Eley, J. A., and Bleeg, J. M., "CFD Investigation of Aeromechanics," ASME Paper 2001-GT-0267, 2001.